Supplementary Information for:

The Temperature Dependence of the Helical Twist of DNA

Franziska Kriegel[1], Christian Matek[2], Tomáš Geršata[3], Klara Kulenkampff[1], Sophie Tschirpke[1], Martin Zacharias[4], Filip Lankaš[3,⋆], and Jan Lipfert [1,⋆]

[1]Department of Physics, Nanosystems Initiative Munich, and Center for Nanoscience, LMU Munich, Amalienstr. 54, 80799 Munich, Germany

[2]Technical University Munich and Institute of Computational Biology, Helmholtz Zentrum Munich-German Research Center for Environmental Health, Ingolstädter Landstr. 1, 85764 Neuherberg, Germany

[3]Department of Informatics and Chemistry, University of Chemistry and Technology Prague, Technická 5, 166 28 Prague, Czech Republic

[4]Physik-Department T38, Technical University of Munich, James-Franck-Strasse, 85748 Garching, Germany

⋆To whom correspondence should be addressed:
Filip Lankaš; Email: lankasf@vscht.cz; Phone: +420-220-44-4392
Jan Lipfert; Email: Jan.Lipfert@lmu.de; Phone: +49-89-2180-2005

Supplementary Figures:

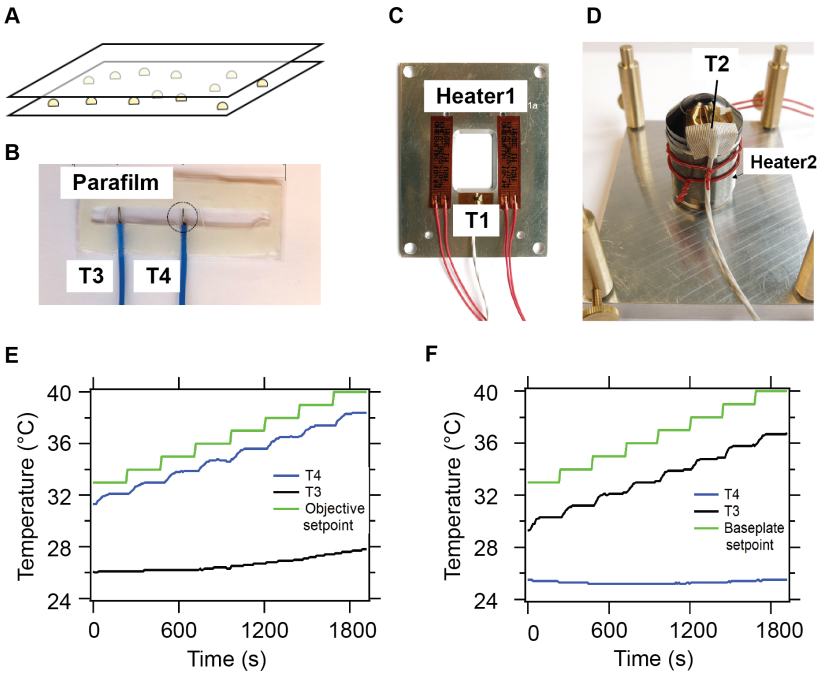

Supplementary Figure 1: Temperature control hardware and measurements. (A) Schematic of surface attached plastic beads that are used as reference beads for the measurements in the MT setup to determine the expansion coefficient of the objective. (B) Image of the custom-made flow cell for temperature measurements. This flow cell uses several parafilm layers as spacers to facilitate insertion of thermocouple temperature sensors (labeled T3 and T4 in the figure). In contrast, our regular flow cells use a single layer of parafilm as spacer. T4 was adjusted such that it is directly above the heated objective; T3 is placed close to the flow cell edge. (C) Image of the two heating foils mounted onto the base plate of the flow cell holder; Thermocouple T1 serves as feedback sensor for this heating circuit. (D) Image of the heating foil mounted on the objective, with temperature sensor T2 that serves as feedback sensor for the objective heating circuit. (E) Temperature readings as a function of time during objective heating only. The green line shows the set temperature, whereas the blue line corresponds to the sensor T4 in the middle of the flow cell. The black line shows the measurements from sensor T3, located at the edge of the flow cell. The difference between set temperature and measured temperature within the FC is about 1 °C. (F) Temperature readings as a function of time during base plate heating only. Same color code as in E. Sensor T4 is almost not affected by heating. The difference between set temperature and measured temperature within the FC is about 2 °C. The offset between the measured temperatures in the flow cell (T3 and T4) and the set temperatures (green lines) is mainly due to the thickness of the flow cell and the fact that it has holes in the top glass cover slip. This offset is avoided when using the regular, thinner flow cell (see Supplementary Figure 2).

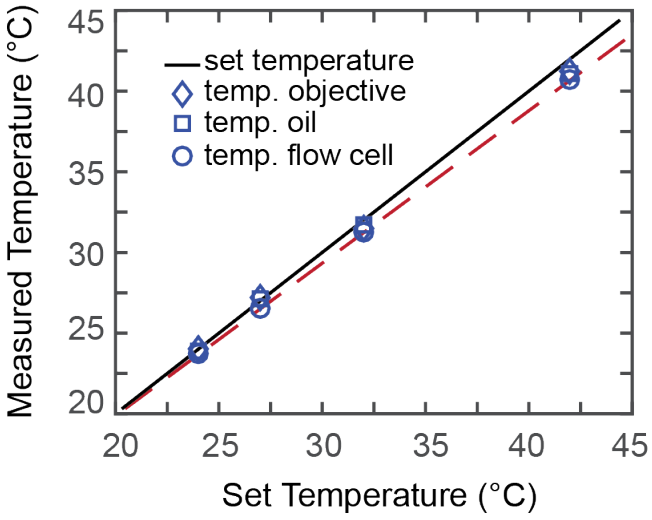

Supplementary Figure 2: Temperature measurements for objective heating only. Measured temperature in the flow cell using the heated objective and regular flow cells with only a single parafilm layer spacer. In contrast to the system in Supplementary Figure 1, we used top glass cover slips with holes such that we can introduce the temperature sensor from the top directly into the solution. The black line indicates the set temperature (the set point at the PID controller). The temperature was measured separately at three positions: in the flow cell (directly at the position of the objective, blue circles), in the oil (between objective lens and flow cell, blue squares) and at the objective (close to the heating foil, blue triangles). The measured temperatures at the objective and in the immersion oil are in excellent agreement with the set point temperature. A slight temperature decrease in the flow cell is observed compared to the set point temperature at the PID. This deviation becomes larger for higher temperatures. Fitting a straight line to the recorded data of the measured temperature within the flow cell vs. set temperature (red, dashed line), we find a deviation of the temperature within the flow cell compared to the set temperature of 6% in °C. From this relation we can calculate which temperature to set in order to reach the wanted temperature within the flow cell. Overall, in the range presented in this work, we reach the temperatures within 0.5 °C.

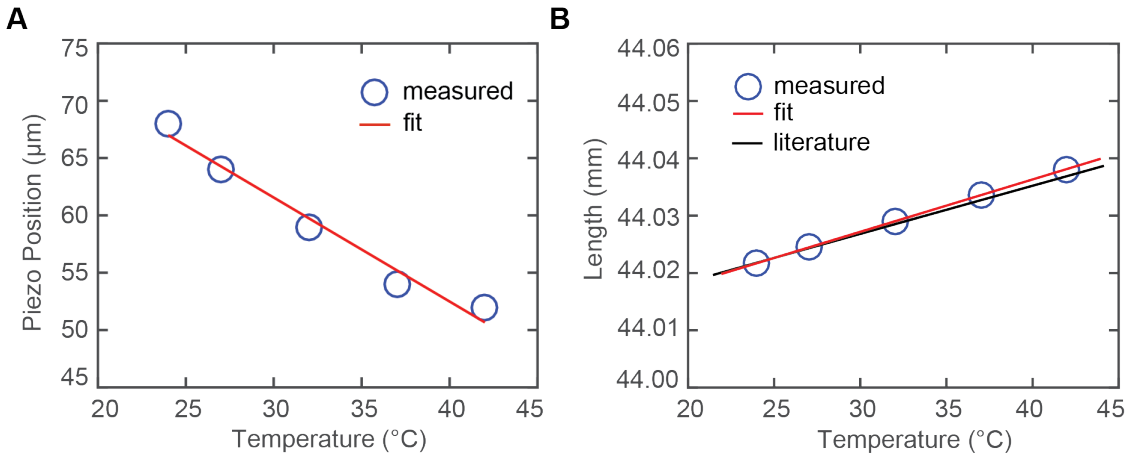

Supplementary Figure 3: Thermal expansion of the objective. The flow cell is pushed upwards upon heating due to the expansion of the objective. This effect can be quantified by tracking the diffraction patterns of surface attached reference beads in the flow cell. (A) The objective is mounted on a piezo and the piezo position was adjusted to keep the diffraction patterns constant while increasing temperature. Shown as blue symbols is the absolute piezo position with increasing temperature. The red solid line is a linear fit to the observed data and its slope can be converted to an apparent expansion coefficient α of the objective, using its length L (L = 44 mm, vendor specification), ΔL and ΔT, by $\alpha = L \cdot \frac{\Delta L}{\Delta T}$. The data shown are for a 60x objective (Olympus, Oil Immersion objective, 60x magnification, NA 1.42,) and imply an expansion coefficient of $(2.06 \pm 0.02) \cdot 10^{-5}\ °C^{-1}$. Similar measurements using a 100x objective (Olympus, Oil Immersion Objective, 100x magnification, NA 1.25) found a thermal expansion coefficient of $(1.8 \pm 0.03) \cdot 10^{-5}\ °C^{-1}$, where the error comes from the error given with the line fit. Both values are very close to the literature value for brass α (brass) $= 1.9 \cdot 10^{-5}\ °C^{-1}$ (http://www.engineeringtoolbox.com/linear-expansion-coefficients-d95.html). (B) The measured length of our objective at room temperature is approximately 44.02 mm. In B, we add the measured expansion (ΔL) to the overall length of the objective and plot the expansion over temperature. Co-plotted is the expansion of the objective using the literature value for the expansion of brass. Good agreement between both lines suggests that the expansion of the brass body of the objective is the dominant effect (compared to e.g. the expansion of the lens or the immersion oil).

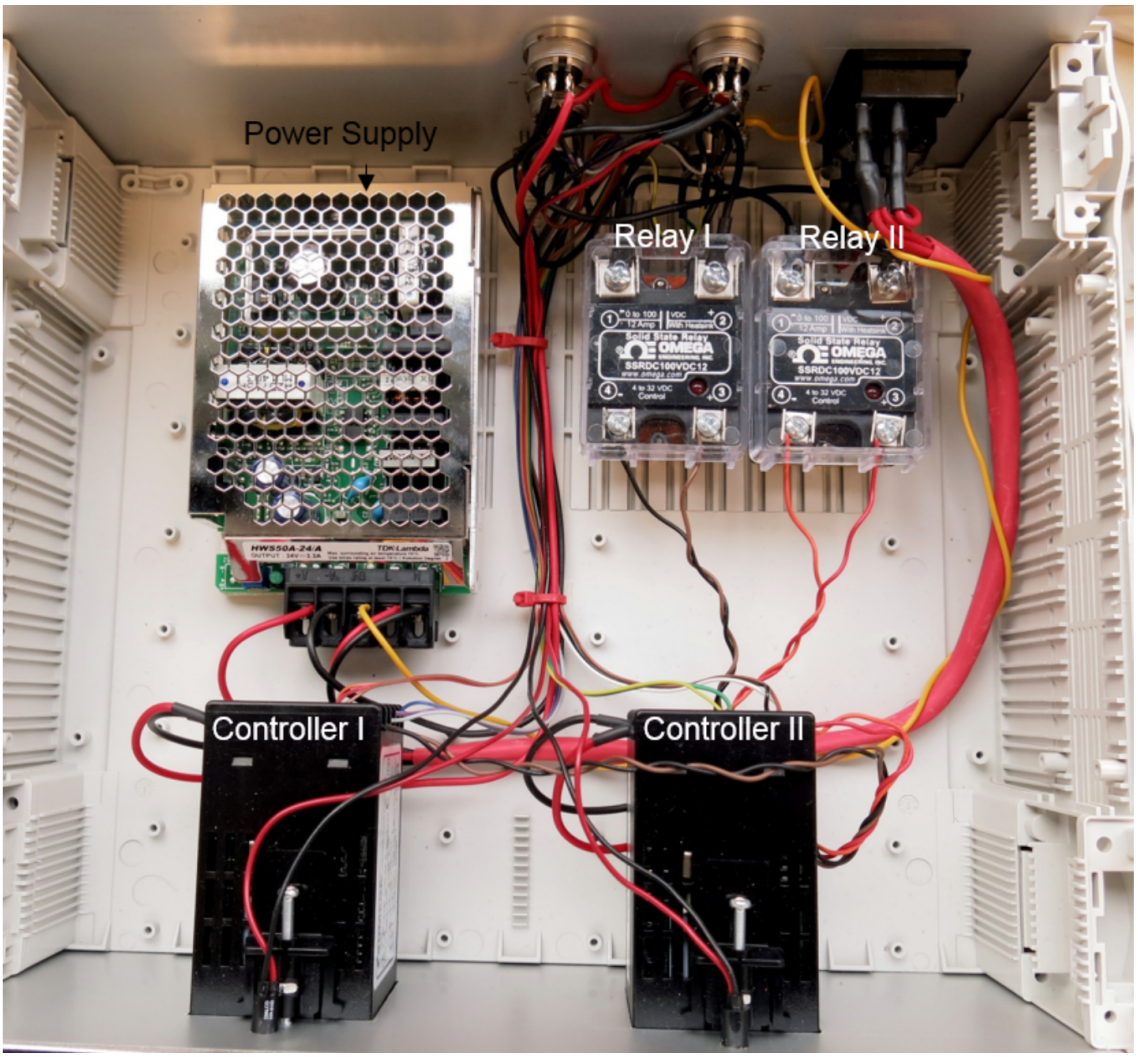

Supplementary Figure 4: Custom made heated circuit for temperature control. The setup has two heating circuits, one for the objective and one for the flow cell heating. Each heating circuit is controlled by a single PID controller: objective heating with Controller 1 and baseplate heating with Controller 2 (as indicated in the figure). The power supply feeds both controllers that are connected to a relay and the temperature sensors.

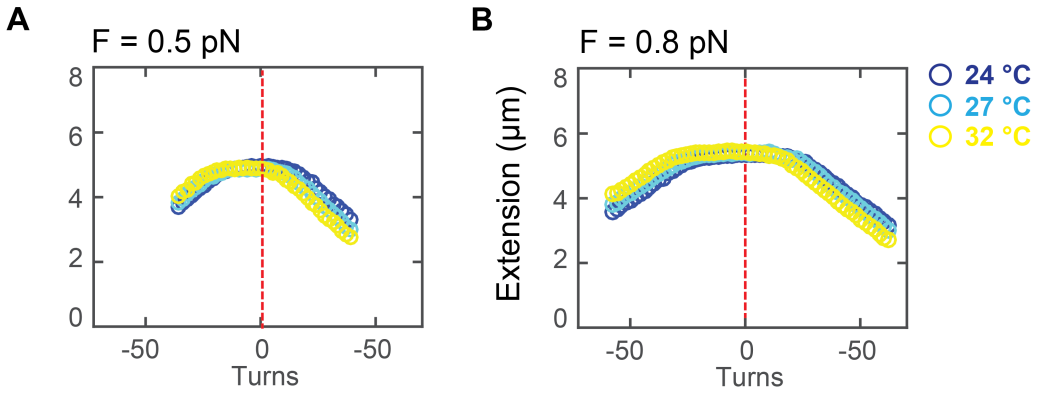

Supplementary Figure 5: Rotation-extension curves for 20.6 kbp DNA. Examples of rotation-extension curves of 20.6 kbp DNA in PBS buffer measured at F = 0.5 and 0.8 pN at 24 °C, 27 °C and 32 °C. We find similar results for 20.6 kbp DNA as for the 7.9 kbp data shown in the main text: the rotation-extension curves shift to negative number of turns with increasing temperature.

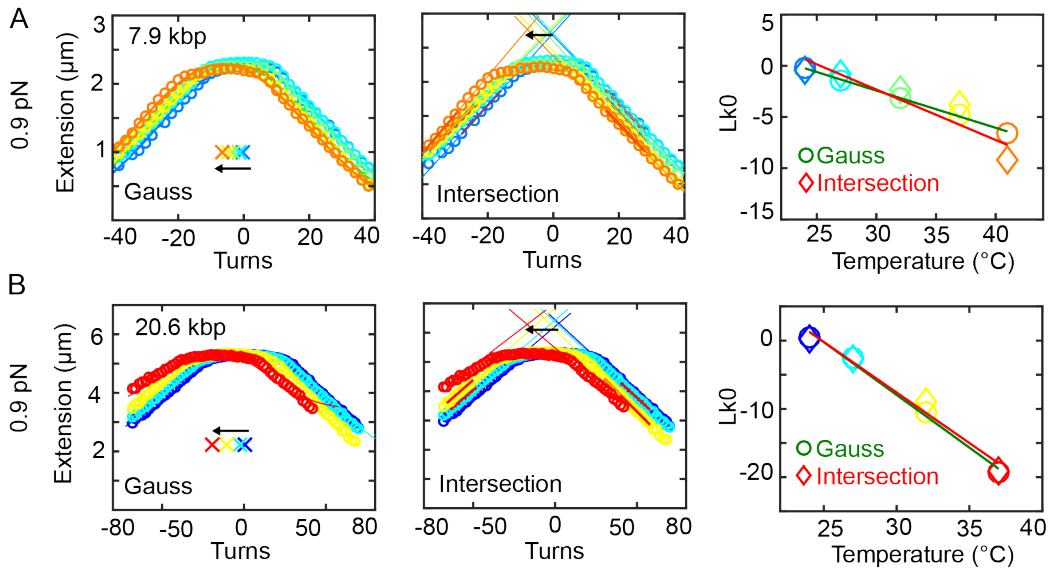

Supplementary Figure 6: Extension-Rotation data at 0.9 pN and different temperatures for a 7.9 kbp (A) and 20.6 kbp DNA molecule (B). Both methods (Gauss fit, left and intersection, middle) give almost identical results (most right column) for the shift in helical twist of DNA with temperature.

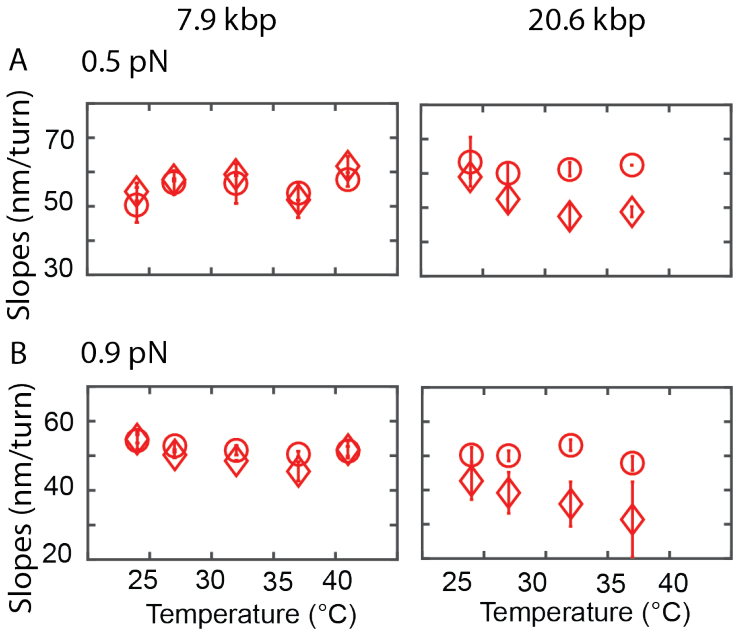

Supplementary Figure 7: Post-buckling slopes at different temperatures for 7.9 kbp DNA (left column) and 20.6 kbp DNA (right column) and at 0.5 pN (A) and 0.9 pN (B). Slopes extracted at positive numbers are illustrated by circles, slopes extracted at a negative number of turns are illustrated with diamonds. Data are taken in PBS and for three molecules.

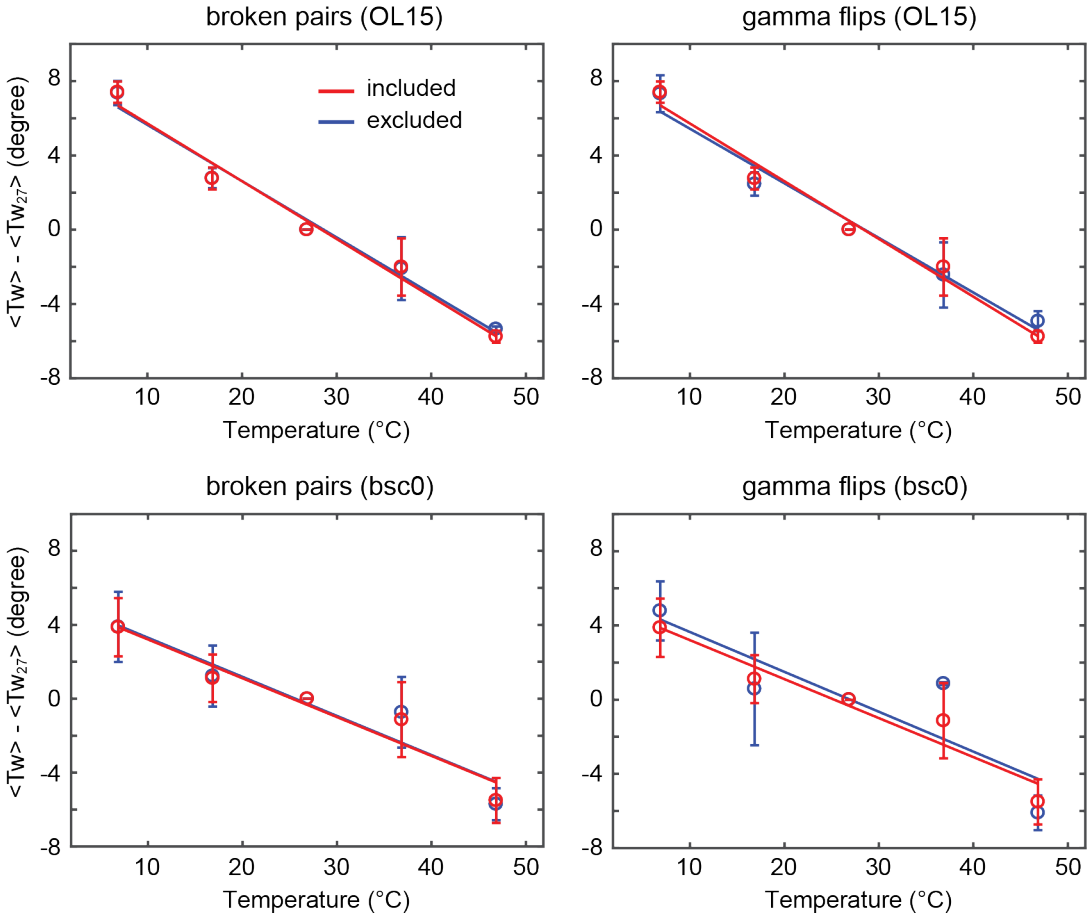

Supplementary Figure 8: Effect of the broken base pairs (left) and the noncanonical flips of the backbone angle gamma (right) on the temperature dependent twist. Excluding snapshots with at least one base pair broken or with at least one gamma flipped (blue) does not change the twist temperature dependence in any significant way compared to the full MD data (red). Top figures illustrate MD simulations performed with the OL15 force field, whereas bottom figures illustrate simulations with the bsc0 force field.

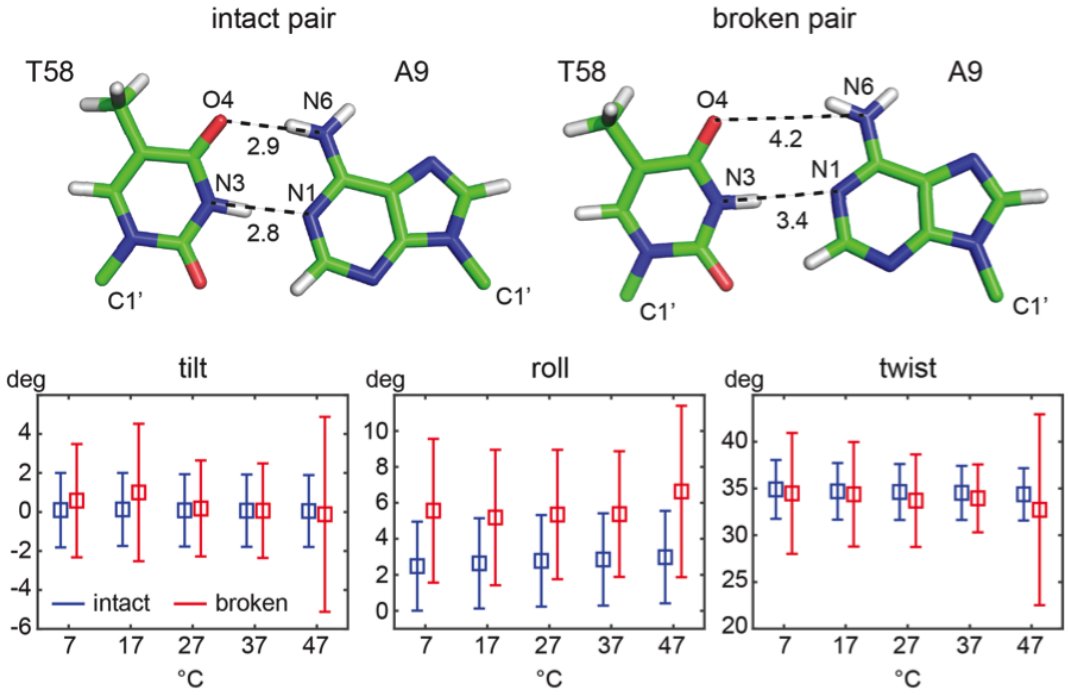

Supplementary Figure 9: Structural effects of a broken pair. We define a pair in MD simulations as broken if at least one of the distances between heavy atoms in a Watson-Crick hydrogen bond exceeds 4 Å. The structures in the upper part were chosen from the intact (left) and broken (right) structural ensemble to exhibit intra-basepair and step coordinates closest to the mean. Distances are in Å. A broken pair is typically only slightly open towards the major groove. Its effect on the basepair step geometry is depicted in the lower part of the Figure, where averages and standard deviations computed from trajectory means for individual steps involving both pairs intact (blue) and at least one pair broken (red) are shown. It is seen that a broken pair induces a slight increase in roll and decrease in twist, while tilt remains nearly unchanged. Broken pairs are mostly isolated, the number of structures where two adjacent pairs are broken simultaneously is negligible. Lifetimes of broken pairs are typically on the order of tens of ps, although rare breaks up to 2700 ps long have been observed.

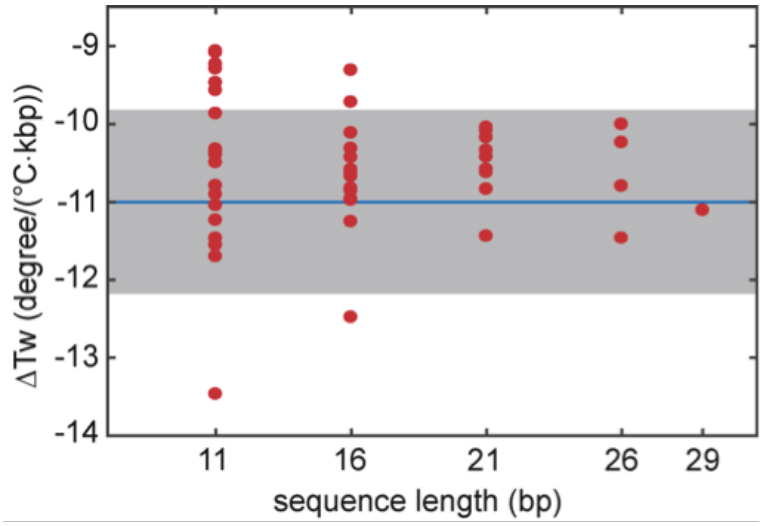

Supplementary Figure 10: Twist temperature change for various subsequences of the 33 bp sequence simulated using atomistic MD. Values for all the subsequences of 1, 1.5, 2 and 2.5 helical turns (11, 16, 21 and 26 bp) together with the full sequence are shown (sequence ends are omitted, see the main text). Starting from 2 helical turns (21 bp), all the values agree with experimental result of this work (blue line), within experimental error (grey zone).

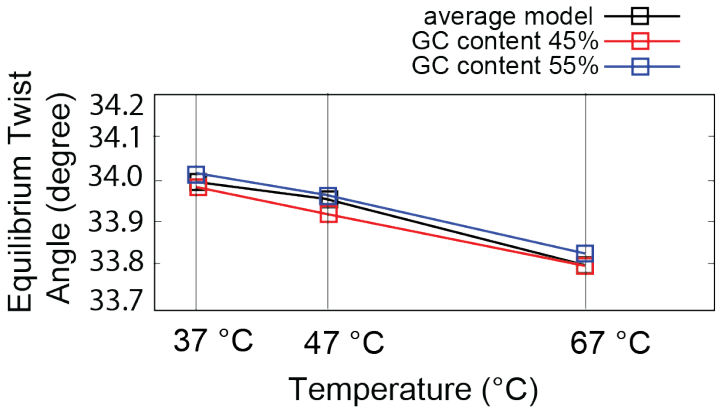

Supplementary Figure 11: Control calculations with the sequence dependent parameterization of oxDNA. In order to check for the effect of varying GC content, we also performed simulations using the sequence-dependent parameterization of oxDNA on a 600-bp system with random sequences of a GC content of 45 and 55 percent. The value of the unwinding constant obtained from both these simulations is -6 degree/(°C·kbp), exhibiting no significant difference to the average base parametrization.

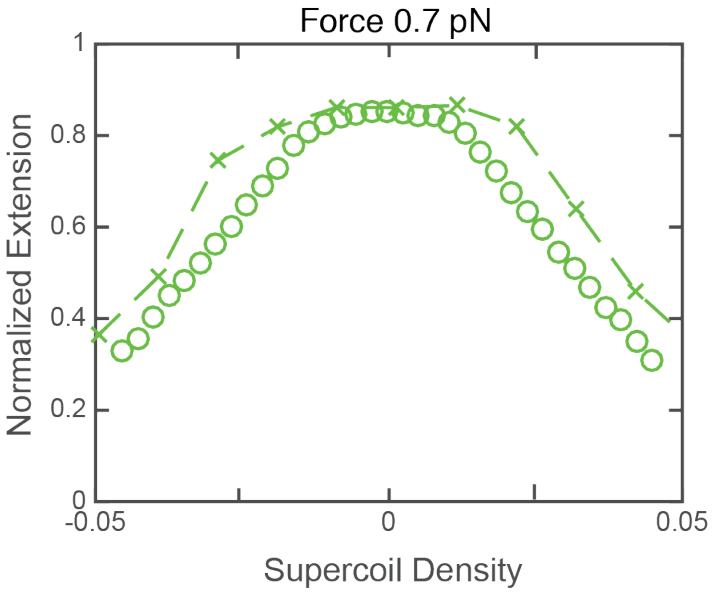

Supplementary Figure 12: Rotation-extension data from MT measurements (circles) and oxDNA simluations (dashed line) at 0.7 pN and at 37 °C. The overall shape of the curve as well as post-buckling slopes, are in good agreement. We note that differences in the precise location of the buckling superhelical density can be rationalized as a finite size effect (1, 2).

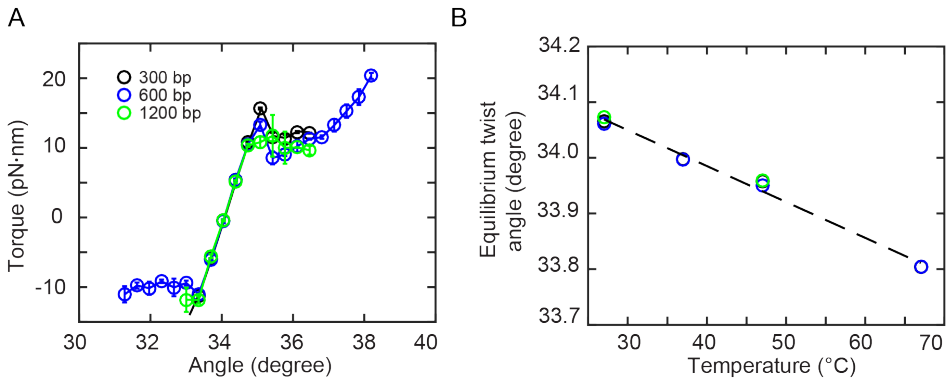

Supplementary Figure 13: Length-dependence of oxDNA results, shown for 300 bp, 600 bp and 1200 bp systems: (A) Torque response curves show identical behavior in the linear regime, while known finite size effects such as buckling overshoot and post-buckling torque increase (1, 2) are more pronounced for smaller systems. (B) Equilibrium twist angle calculated from fit to the linear regime of the torque response curve show no significant length-dependence.

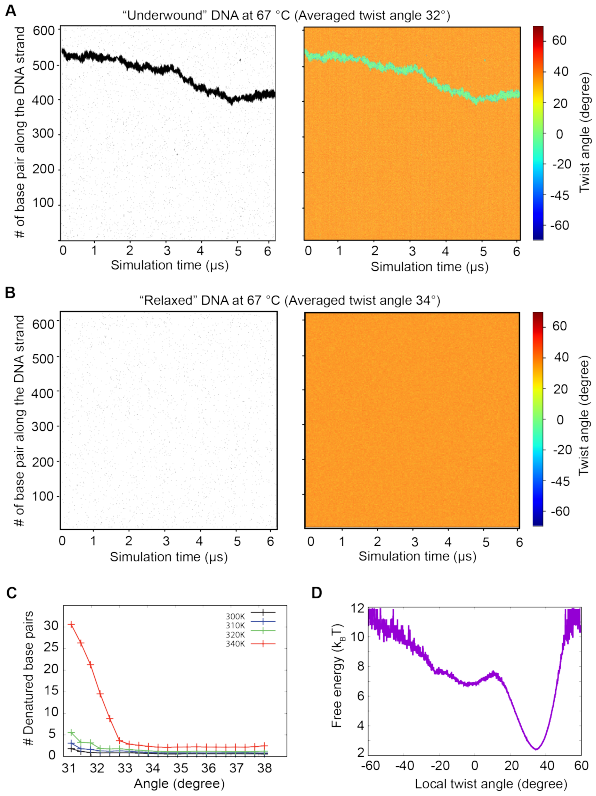

Supplementary Figure 14: Analysis of DNA melting in oxDNA simulations of a 600 bp DNA molecule using the average-base parametrization. Base-pair denaturation in oxDNA is defined by an interaction energy cutoff as explained in the main text. The local twist angle between two consecutive base pairs is measured by calculating the vectors connecting the centers of mass of the bases on opposite strands involved in both base pairs, and measuring the angle between these two vectors when projected into a plane perpendicular to the line connecting the center points of the consecutive base pairs. (A) Kymographs of base-pair denaturation (left) and local twist angle (right) for a system torsionally constrained to an average twist angle of 32.0°, corresponding to a supercoiling density of $\sigma = -0.059$. Comparing the kymographs shows that the undertwist is localized, while the double-stranded region retains its relaxed-twist value. (B) Denaturation and local twist angle kymograph for a system torsionally constrained to an average twist angle of 34.0°, corresponding to a supercoiling density of $\sigma \sim 0$. The kymograph demonstrates short-lived and delocalized opening of double-strand base-pairs due to thermal fluctuations. The delocalized and short-lived nature of the base pair opening events leads to the appearance of (very) subtle "speckles" in the graph. (C) Number of denatured base pairs as a function of average twist angle and temperature. (D) Free energy landscape of local twist angles for T = 67 °C and an average twist angle of 32.0°. The free energy landscape exhibits a global minimum at ∼34°, corresponding to the base paired helix and a secondary minimum at ∼0°, corresponding to denatured base pairs.

Supplementary Tables:

	OL15 in degree/°C·kbp	**bsc0 in degree/°C·kbp**
End-to-end mean-plane	-11.1±0.3	-7.5±0.17
End-to-end axis-angle	-10.1±0.2 to -11.3±0.2	-6.3±0.15 to -8.0±0.19
Helical twist 3DNA	-7.6±0.2	-2.6±0.7
Helical twist Curves+	-10.5±0.1	-5.0±0.9
Local twist 3DNA	-12.2±0.1	-6.3±0.8
Local twist Curves+	-12.4±0.1	-6.4±0.8

Supplementary Table 1: Collection of slopes for the change in helical twist obtained from MD data. Values for the OL15 and for the bsc0 Amber force fields are shown in degree/°C·kbp. Various twist definitions have been used. The end-to-end twist is based on the two end frames (Figure 2 in the main text). The mean-plane twist is invariant with respect to constant offset rotation of the end frames around their Z-axes, as proved in this Supplementary Information. The axis-angle twist varies somewhat with the offset rotation and we show the interval of values for a series of rotations in 45 degree steps. Temperature slopes of end-to-end twists for each force field are mutually consistent irrespective of the definition and expose the differences between the force fields. The OL15 values agree quantitatively with the experiment, whereas the bsc0 values are lower. For completeness, results for twist defined as a sum of helical or local base pair step twists along the oligomer are also shown. The values span a wide range depending on the details of the definition.

ΔT_w(T) in degree/°C·kbp	Method	Reference
-10 to -11	Plasmid ligation and gel-electrophoresis, T = 60-100 °C	Depew and Wang, Ref. (3)
-10.5	Plasmid ligation and gel-electrophoresis, T = 35-83 °C	Duguet, Ref. (4)
-13.4	Magnetic tweezers, 48 kbp λ-DNA, T = 27-42 °C	Strick et al., Ref. (5)
-10.5 ± 0.6	Magnetic tweezers, 7.9 kbp DNA, T = 24-42 °C	This work
-11.5 ± 1.0	Magnetic tweezers, 20.6 kbp DNA, T = 24-42 °C	This work
-6.5	MD simulations	Everaers and co-workers, Ref. (6)
-10.8 ± 0.1	MD simulations, mean-plane definition, OL15, T = 7-47 °C	This work
-6.4 ± 0.2	oxDNA simulations, T = 27-67 °C	This work

Supplementary Table 2: Values for the change of DNA twist with temperature ΔT_w(T) from measurements and simulations. Early experiments using plasmid ligation and gel-electrophoresis derived values similar to the determined values within this work. The value obtained by Strick et. al. using MT is slightly higher. Everaers and co-workers published a value for the change in helical twist using MD simulations that is half the determined experimental values. MD calculations presented in this work using the OL15 force field refer values similar to the experimental data. Using the oxDNA frame work results in values half the experimental values. Further discussion is in the main text.

Supplementary Methods: Rotational offset invariance

In this part we show that if one uses the mean plane definition of the end-to-end twist (i.e. the twist definition employed in 3DNA), then the change of the ensemble averaged end-to-end twist with temperature (or with any other set of conditions) is independent of the fixed rotations of the end frames about their z-axes.

General rotation matrix

Let $R_{\mathbf{u}}(\phi)$ denote a general rotation matrix describing a rotation of magnitude ϕ about an arbitrary unit vector $\mathbf{u}$

$$R_{\mathbf{u}}(\phi) = \begin{pmatrix} \cos\phi + (1-\cos\phi)u_x^2 & (1-\cos\phi)u_x u_y - u_z \sin\phi & (1-\cos\phi)u_x u_z + u_y \sin\phi \\ (1-\cos\phi)u_x u_y + u_z \sin\phi & \cos\phi + (1-\cos\phi)u_y^2 & (1-\cos\phi)u_y u_z - u_x \sin\phi \\ (1-\cos\phi)u_x u_z - u_y \sin\phi & (1-\cos\phi)u_y u_z + u_x \sin\phi & \cos\phi + (1-\cos\phi)u_z^2 \end{pmatrix} \tag{9}$$

Mean-plane twist

Let $\{\hat{\mathbf{d}}_i^1\}$ and $\{\hat{\mathbf{d}}_i^2\}$ $(i = x, y, z)$ be the two right-handed orthonormal end-frames. The z-axes define the hinge axis $\hat{\mathbf{h}}$,

$$\hat{\mathbf{h}} = \hat{\mathbf{d}}_z^1 \times \hat{\mathbf{d}}_z^2, \tag{10}$$

and the net bending angle $\hat{\Lambda}$,

$$\hat{\Lambda} = \arccos(\hat{\mathbf{d}}_z^1 \cdot \hat{\mathbf{d}}_z^2). \tag{11}$$

To obtain the mean-plane twist, the first frame is rotated by $\hat{\Lambda}/2$,

$$\hat{\mathbf{g}}_i^1 = R_{\hat{\mathbf{h}}}(\hat{\Lambda}/2)\hat{\mathbf{d}}_i^1, \ i = x, y, z \tag{12}$$

and the second frame by $-\hat{\Lambda}/2$,

$$\hat{\mathbf{g}}_i^2 = R_{\hat{\mathbf{h}}}(-\hat{\Lambda}/2)\hat{\mathbf{d}}_i^2, \ i = x, y, z \tag{13}$$

about the hinge axis $\hat{\mathbf{h}}$, so that the resulting x and y axes of both frames $\{\hat{\mathbf{g}}_i^1\}$ and $\{\hat{\mathbf{g}}_i^2\}$ lie in the same plane perpendicular to the z-axes. The mean-plane twist is then defined as

$$\hat{t} = \arccos(\hat{\mathbf{g}}_y^1 \cdot \hat{\mathbf{g}}_y^2)\mathrm{sgn}([\hat{\mathbf{g}}_y^1 \times \hat{\mathbf{g}}_y^2] \cdot \hat{\mathbf{g}}_z^1), \tag{14}$$

where sgn(.) is the signum function.

Middle frame

We further define a middle frame $\{\mathbf{m}_i\}(i = x, y, z)$ so that $\mathbf{m}_z = \hat{\mathbf{g}}_z^1$ and $\mathbf{m}_i, \ i = x, y$ lie symmetrically between the corresponding $\hat{\mathbf{g}}_i^1$ and $\hat{\mathbf{g}}_i^2$. The middle frame is by definition right-handed and orthonormal. Since twist is the signed angle between $\hat{\mathbf{g}}_y^1$ and $\hat{\mathbf{g}}_y^2$, it follows that

$$\begin{aligned} \hat{\mathbf{g}}_y^1 &= R_{\mathbf{m}_z}(-\hat{t}/2)\mathbf{m}_y \\ \hat{\mathbf{g}}_y^2 &= R_{\mathbf{m}_z}(\hat{t}/2)\mathbf{m}_y. \end{aligned} \tag{15}$$

Since the hinge axis $\hat{\mathbf{h}}$ is perpendicular to $\mathbf{m}_z$, we can write

$$\hat{\mathbf{h}} = R_{\mathbf{m}_z}(\varphi)\mathbf{m}_y, \tag{16}$$

where we have introduced φ as an angle between $\hat{\mathbf{h}}$ and $\mathbf{m}_y$.

Offset rotation of the end-frames

If we rotate $\{\hat{\mathbf{d}}_i^1\}$ by a fixed angle ψ_1 about $\hat{\mathbf{d}}_z^1$,

$$\mathbf{d}_i^1 = R_{\hat{\mathbf{d}}_z^1}(\psi_1)\hat{\mathbf{d}}_i^1,\ i = x, y, z \tag{17}$$

and $\{\hat{\mathbf{d}}_i^2\}$ by a fixed angle ψ_2 about $\hat{\mathbf{d}}_z^2$,

$$\mathbf{d}_i^2 = R_{\hat{\mathbf{d}}_z^2}(\psi_2)\hat{\mathbf{d}}_i^2,\ i = x, y, z \tag{18}$$

the value of twist changes to

$$t = \arccos(\mathbf{g}_y^1 \cdot \mathbf{g}_y^2)\mathrm{sgn}([\mathbf{g}_y^1 \times \mathbf{g}_y^2] \cdot \mathbf{g}_z^1), \tag{19}$$

where

$$\begin{array}{l} \mathbf{g}_i^1 = R_{\mathbf{h}}(\Lambda/2)\mathbf{d}_i^1, \\ \mathbf{g}_i^2 = R_{\mathbf{h}}(-\Lambda/2)\mathbf{d}_i^2,\ i = 1, 2, 3\ \ , \end{array} \tag{20}$$

and $\mathbf{h}$ and Λ are defined in the same way as (10) and (11),

$$\begin{array}{l} \mathbf{h} = \mathbf{d}_z^1 \times \mathbf{d}_z^2, \\ \Lambda = \arccos(\mathbf{d}_z^1 \cdot \mathbf{d}_z^2). \end{array} \tag{21}$$

The z-axes remain unchanged by the rotation, so that $\mathbf{d}_z^1 = \hat{\mathbf{d}}_z^1$, $\mathbf{d}_z^2 = \hat{\mathbf{d}}_z^2$. Thus from the definition $\Lambda = \hat{\Lambda}$ and $\mathbf{h} = \hat{\mathbf{h}}$ and consequently also $\mathbf{g}_z^1 = \hat{\mathbf{g}}_z^1$, $\mathbf{g}_z^2 = \hat{\mathbf{g}}_z^2$.

As the next step we express the vectors $\mathbf{g}_y^1$, $\mathbf{g}_y^2$ and $\mathbf{g}_z^1$, used to define the twist t, as functions of only $\mathbf{m}_i,\ i = x, y$ and angles Λ, φ, ψ_1 and ψ_2. We have

$$\begin{array}{l} \mathbf{g}_y^1 = R_{\hat{\mathbf{h}}}(\Lambda/2)R_{\hat{\mathbf{d}}_z^1}(\psi_1)R_{\hat{\mathbf{h}}}(-\Lambda/2)\hat{\mathbf{g}}_y^1 \\ \mathbf{g}_y^2 = R_{\hat{\mathbf{h}}}(-\Lambda/2)R_{\hat{\mathbf{d}}_z^2}(\psi_2)R_{\hat{\mathbf{h}}}(\Lambda/2)\hat{\mathbf{g}}_y^2 \\ \mathbf{g}_z^1 = \hat{\mathbf{g}}_z^1, \end{array} \tag{22}$$

where

$$\begin{array}{l} \hat{\mathbf{d}}_z^1 = R_{\hat{\mathbf{h}}}(-\Lambda/2)\hat{\mathbf{g}}_z^1 \\ \hat{\mathbf{d}}_z^2 = R_{\hat{\mathbf{h}}}(\Lambda/2)\hat{\mathbf{g}}_z^1 \end{array} \tag{23}$$

Finally, we substitute for $\hat{\mathbf{g}}_y^1$ and $\hat{\mathbf{g}}_y^2$ from (15) and for $\hat{\mathbf{h}}$ from (16), and use the fact that $\hat{\mathbf{g}}_z^1 = \mathbf{m}_z$ by definition. Thus, all the vectors in (22) are now expressed as composed rotations of the vectors $\mathbf{m}_i$, $i = x, y$ of the middle frame,

$$\begin{array}{l} \mathbf{g}_y^1 = R_{\hat{\mathbf{h}}}(\Lambda/2)R_{\hat{\mathbf{d}}_z^1}(\psi_1)R_{\hat{\mathbf{h}}}(-\Lambda/2)R_{\mathbf{m}_z}(-\hat{t}/2)\mathbf{m}_y \\ \mathbf{g}_y^2 = R_{\hat{\mathbf{h}}}(-\Lambda/2)R_{\hat{\mathbf{d}}_z^2}(\psi_2)R_{\hat{\mathbf{h}}}(\Lambda/2)R_{\mathbf{m}_z}(\hat{t}/2)\mathbf{m}_y \\ \mathbf{g}_z^1 = \mathbf{m}_z, \end{array} \tag{24}$$

where

$$\begin{aligned}\hat{\mathbf{d}}_z^1 &= R_{\hat{\mathbf{h}}}(-\Lambda/2)\mathbf{m}_z \\ \hat{\mathbf{d}}_z^2 &= R_{\hat{\mathbf{h}}}(\Lambda/2)\mathbf{m}_z \\ \hat{\mathbf{h}} &= R_{\mathbf{m}_z}(\varphi)\mathbf{m}_y.\end{aligned} \tag{25}$$

We now substitute for $\mathbf{g}_y^1$, $\mathbf{g}_y^2$ and $\mathbf{g}_z^1$ in the definition of twist (19) from (24) and simplify the result in coordinate representation, with $\{\mathbf{m}_i\}$ taken as the basis. Λ, φ, $\hat{t}$, ψ_1 and ψ_2 are considered to be parameters. This leads to

$$t = \hat{t} - \psi_1 + \psi_2, \tag{26}$$

for $-\pi < \hat{t} - \psi_1 + \psi_2 \leq \pi$. Thus, fixed rotations of the end frames about their z-axes change the twist simply by the difference of the two rotation angles, namely $\psi_2 - \psi_1$. Consider now two temperatures, T_1 and T_2. It follows from (26) that

$$\begin{aligned}\langle t \rangle_{T_1} &= \langle \hat{t} \rangle_{T_1} - \psi_1 + \psi_2, \\ \langle t \rangle_{T_2} &= \langle \hat{t} \rangle_{T_2} - \psi_1 + \psi_2,\end{aligned} \tag{27}$$

and therefore

$$\langle t \rangle_{T_2} - \langle t \rangle_{T_1} = \langle \hat{t} \rangle_{T_2} - \langle \hat{t} \rangle_{T_1} \tag{28}$$

which proves the desired invariance with respect to the offset rotation.

References

1. H Brutzer, N Luzzietti, D Klaue, and R Seidel. Energetics at the DNA supercoiling transition. *Biophysical Journal*, 98(7):1267–1276, 2010.

2. C Matek, T E Ouldridge, J P K Doye, and A Louis. Plectoneme tip bubbles: coupled denaturation and writhing in supercoiled DNA. *Scientific Reports*, 5(1):7655, 2015.

3. D E Depew and J C Wang. Conformational fluctuations of DNA helix. *Proceedings of the National Academy of Sciences of the United States of America*, 72(11):4275–4279, 1975.

4. M Duguet. The helical repeat of DNA at high temperature. *Nucleic acids research*, 21(3):463–8, 1993.

5. T R Strick, V Croquette, and D Bensimon. Homologous pairing in stretched supercoiled DNA. *Proceedings of the National Academy of Sciences of the United States of America*, 95(18):10579–10583, 1998.

6. S Meyer, D Jost, N Theodorakopoulos, M Peyrard, R Lavery, and R Everaers. Temperature dependence of the DNA double helix at the nanoscale: structure, elasticity, and fluctuations. *Biophysical Journal*, 105(8):1904–1914, 2013.